Geochemistry Geophysics Geosystems G3

Article
Volume 11, Number 5
13 May 2010
Q05W05, doi:10.1029/2009GC002970
ISSN: 1525-2027

Published by AGU and the Geochemical Society

Constraints on lithosphere net rotation and asthenospheric viscosity from global mantle flow models and seismic anisotropy

Clinton P. Conrad
Department of Geology and Geophysics, University of Hawai'i at Mānoa, Honolulu, Hawaii 96822, USA (clintc@hawaii.edu)

Mark D. Behn
Department of Geology and Geophysics, Woods Hole Oceanographic Institution, Woods Hole, Massachusetts 02543, USA

[1] Although an average westward rotation of the Earth's lithosphere is indicated by global analyses of surface features tied to the deep mantle (e.g., hot spot tracks), the rate of lithospheric drift is uncertain despite its importance to global geodynamics. We use a global viscous flow model to predict asthenospheric anisotropy computed from linear combinations of mantle flow fields driven by relative plate motions, mantle density heterogeneity, and westward lithosphere rotation. By comparing predictions of lattice preferred orientation to asthenospheric anisotropy in oceanic regions inferred from SKS splitting observations and surface wave tomography, we constrain absolute upper mantle viscosity (to 0.5–1.0 × 10^{21} Pa s, consistent with other constraints) simultaneously with net rotation rate and the decrease in the viscosity of the asthenosphere relative to that of the upper mantle. For an asthenosphere 10 times less viscous than the upper mantle, we find that global net rotation must be <0.26°/Myr (<60% of net rotation in the HS3 (Pacific hot spot) reference frame); larger viscosity drops amplify asthenospheric shear associated with net rotation and thus require slower net rotation to fit observed anisotropy. The magnitude of westward net rotation is consistent with lithospheric drift relative to Indo-Atlantic hot spots but is slower than drift in the Pacific hot spot frame (HS3 ≈ 0.44°/Myr). The latter may instead express net rotation relative to the deep mantle beneath the Pacific plate, which is moving rapidly eastward in our models.

Components: 11,400 words, 8 figures, 1 table.

Keywords: net rotation; lithsopheric drift; seismic anisotropy; asthenospheric shear; plate motions; global mantle flow.

Index Terms: 8120 Tectonophysics: Dynamics of lithosphere and mantle: general (1213); 8158 Tectonophysics: Plate motions: present and recent (3040); 8162 Tectonophysics: Rheology: mantle (8033).

Received 19 November 2009; **Revised** 3 March 2010; **Accepted** 26 March 2010; **Published** 13 May 2010.

Conrad, C. P., and M. D. Behn (2010), Constraints on lithosphere net rotation and asthenospheric viscosity from global mantle flow models and seismic anisotropy, *Geochem. Geophys. Geosyst.*, *11*, Q05W05, doi:10.1029/2009GC002970.

Theme: Plate Reconstructions, Mantle Convection, and Tomography Models: A Complementary Vision of Earth's Interior
Guest Editors: D. Muller, S. Quere, and T. Torsvik

1. Introduction

[2] The relative motions between Earth's tectonic plates can be reasonably well constrained by the spacing of parallel magnetic lineations observed on the seafloor [e.g., *Vine and Matthews*, 1963; *Morgan*, 1968]. In fact, modern geodetic observations of plate motions [*Sella et al.*, 2002; *Kreemer et al.*, 2003] show nearly the same patterns and rates of relative motion as early characterizations [e.g., *Chase*, 1972, 1978; *Minster and Jordan*, 1978], with a few notable differences. The motion of the tectonic plates relative to the deep mantle, however, has been the subject of significant uncertainty and debate since the advent of plate tectonics. This is because the appropriate deep-mantle reference frame against which to measure surface plate motions is poorly defined and difficult to characterize. Yet, any net motion of the tectonic plates over the deep mantle has potentially important consequences for the dynamics of mantle slabs [e.g., *Doglioni et al.*, 2007; *Long and Silver*, 2009; *van der Meer et al.*, 2010], the tectonics of trench migration at the surface [*Husson et al.*, 2008; *Nagel et al.*, 2008; *Schellart et al.*, 2008; *Di Giuseppe et al.*, 2009], the coupling between tectonic plates and mantle flow [*Becker*, 2006; *Becker and Faccenna*, 2009], the rise of plumes within the flowing mantle [e.g., *Steinberger*, 2000; *Steinberger et al.*, 2004], and long-term sea level change [*Conrad and Husson*, 2009]. As described below, some of these interactions with absolute plate motions have been used to constrain the lithosphere's net motion relative to the deep mantle. This serves to highlight the need for an independent constraint on absolute plate motions, much as seafloor magnetic lineations serve as an independent constraint on relative plate motions.

[3] Convection in the Earth's mantle, which ultimately drives the plate motions, is inherently poloidal in the absence of lateral viscosity heterogeneity. As a result, a mantle with radially symmetric viscosity will induce no net torques on the lithospheric plates, and therefore no net rotation of the lithosphere [*Solomon and Sleep*, 1974]. Thus, the no–net rotation reference frame (NNR), which can be determined solely from the well-characterized relative motions between plates, forms a natural reference frame within which global plate motions can be expressed [*Argus and Gordon*, 1991]. The Earth's viscosity structure, however, is not radially symmetric, and numerical models have shown that lateral variations in upper mantle viscosity, primarily associated with deep cratonic roots, can induce net lithopshere rotation [*Ricard et al.*, 1991; *Zhong*, 2001; *Becker*, 2006]. Most of these models have predicted a slow net drift of the lithosphere in a direction roughly parallel to that of the Pacific plate [*Becker and Faccenna*, 2009]. Without its no–net torque justification, the NNR frame becomes merely a convenient mathematical construct upon which to express relative plate motions; the NNR frame provides no constraints on the absolute motions of plates relative to the deep mantle. Furthermore, the definition of the NNR frame depends on the details of the plate tectonic model, such as the treatment of diffuse plate boundaries and small plates [*Kreemer et al.*, 2006]. Instead, a geological or geophysical observation that constrains the deep mantle reference frame is needed.

[4] The search for such a constraint is nearly as old as the discovery of plate tectonics itself. Early studies utilized hot spot volcanism as a deep mantle reference frame, assuming it to be the surface expression of stationary plumes rising from the deep mantle [e.g., *Wilson*, 1965; *Morgan*, 1972]. This approach has been used in several plate tectonic compilations [e.g., *Minster and Jordan*, 1978; *Gordon and Jurdy*, 1986; *Gripp and Gordon*, 1990; *Wang and Wang*, 2001]. However, a few cm/yr of relative motion between hot spots have been suggested by plate circuit analyses [*Molnar and Stock*, 1987] and paleomagnetic investigations [*Tarduno and Gee*, 1995; *Tarduno and Cottrell*, 1997; *DiVenere and Kent*, 1999; *Tarduno et al.*, 2003], as well as modeling studies showing that plume tails are advected horizontally by mantle flow [e.g., *Steinberger*, 2000; *O'Neill et al.*, 2005], has called the stability of the hot spot reference frame into question. More recently, groups of hot spots in either the Indo-Atlantic basin [*Müller et al.*, 1993; *O'Neill et al.*, 2005] or in the Pacific basin [*Gripp and Gordon*, 2002; *Wessel et al.*, 2006] have been used to define a reference frame. A similar approach has also been used for a global compilation of hot spots linked via a mantle flow model [*Torsvik et al.*, 2008, 2010].

[5] Relative to the NNR frame, the different hot spot–based reference frames predict a similar direction of net lithosphere motion, but with different rates of net lithosphere drift [*Becker and Faccenna*, 2009]. Nearly all models suggest a net westward rotation of the lithosphere about an Euler pole located in the Southern Indian Ocean. Of seven recent net rotation models (Table 1) and five recent numerical models (Table 1) that produce net

Table 1. Euler Poles for Net Rotation of Earth's Lithosphere in Various Reference Frames Defined by Plate Kinematics, Hot Spot Compilations, Numerical Models of Global Mantle Flow, and Seismic Anisotropy[a]

Model Name	Pole Location: Latitude (°N)	Pole Location: Longitude (°E)	Rotation Rate (°/Myr)	Maximum Drift (cm/yr)	Distance to HS3 Pole (deg)	Reference
			Plate Kinematics			
NNR	NA	NA	0.0	0.0	NA	*Argus and Gordon* [1991][b]
ANT	−63	64	0.25	2.8	7.6	*Hamilton* [2003][c]
AFR	−51	106	0.30	3.3	22	*Burke and Wilson* [1972][c]
			Hot Spots			
HS3	**−56**	**70**	**0.44**	**4.9**	**0**	***Gripp and Gordon* [2002][d]**
HS2	−49	65	0.33	3.7	7.6	*Gripp and Gordon* [1990][d]
SB04	−40	38	0.17	1.9	26	*Steinberger et al.* [2004][d]
GJ86	−30	33	0.11	1.2	37	*Gordon and Jurdy* [1986]
R91h	−56	84	0.15	1.7	7.8	*Ricard et al.* [1991][d]
T22	−62	88	0.14	1.3	11	*Wang and Wang* [2001][e]
T10	−68	132	0.13	1.4	30	*Torsvik et al.* [2010]
ON05	−46	92	0.19	2.1	17	*O'Neill et al.* [2005]
			Flow Models			
R91m	−47	93	0.15	1.7	17	*Ricard et al.* [1991][d]
Z01	−42	103	0.09	1.0	25	*Zhong* [2001][d]
B06a	−46	71	0.08	0.9	10	*Becker* [2006][d]
B06b	−45	94	0.13	1.4	19	*Becker* [2006][d]
BSK	−63	76	0.06	0.7	7.6	*Becker* [2006][d]
			Anisotropic Constraints			
K09	−58	63	0.21	2.3	4.0	*Kreemer* [2009]

[a]Reference frames should be compared to the HS3 (Pacific hot spot) reference frame (in boldface), which we use as a basis for defining the net rotation scale factor α. NA, not applicable.
[b]Net rotation Euler pole is trivial.
[c]Net rotation Euler pole determined from NNR model of *Argus and Gordon* [1991].
[d]Net rotation Euler pole reported by *Becker and Faccenna* [2009].
[e]Net rotation Euler pole reported by *Becker* [2006].

rotation, all rotate around Euler poles that are located within 37° of the (70°E, 56°S) location of the Euler pole for the HS3 net rotation model of *Gripp and Gordon* [2002]. The HS3 net rotation pole is also proximal to the poles for net rotation with respect to the Antarctic and African plates (Table 1), which have each been proposed as stable frames because they are nearly surrounded by ridges [*Burke and Wilson*, 1972; *Hamilton*, 2003]. By contrast, the amplitude of the net rotation is dramatically different between the various reference frames, varying by a factor of 4 between a minimum of 0.11°/Myr for the GJ86 model [*Gordon and Jurdy*, 1986] and 0.44°/Myr for the HS3 (Pacific Hot spots) model [*Gripp and Gordon*, 2002] (Table 1). In terms of net lithospheric motion, these two extreme models produce between 1.2 and 4.9 cm/yr (Table 1) of net lithosphere rotation (on the equator of the rotation) in an approximately westward direction that is roughly parallel to Pacific plate motion. Thus, hot spot models appear to produce a relatively consistent constraint on the westward direction of net rotation, but a comparatively poor constraint on the magnitude of this net rotation.

[6] *Becker* [2008] suggested that observations of seismic anisotropy in the asthenosphere could provide a separate constraint on the net motion of the lithosphere relative to the deep mantle. The asthenosphere is a low-viscosity sublithospheric layer that accommodates relative motion between the tectonic plates and upper mantle flow. This deformation occurs primarily by dislocation creep in the asthenosphere [*Karato and Wu*, 1993], which aligns olivine crystals with a lattice preferred orientation (LPO) [*McKenzie*, 1979; *Ribe*, 1989] that can be detected seismically [e.g., *Hess*, 1964; *Montagner*, 1994] using surface waves [e.g., *Trampert and Woodhouse*, 2003; *Becker et al.*, 2003; *Debayle et al.*, 2005] or shear wave splitting measurements [e.g., *Silver and Chan*, 1988; *Savage*, 1999]. Thus, seismic anisotropy in the asthenosphere is controlled by the motion of the lithosphere relative to that of the underlying mantle [e.g., *Savage*, 1999]. Because net rotation of the

lithosphere over the deep mantle is one component of asthenospheric deformation, seismic anisotropy can be used to constrain absolute plate motion if other components associated with relative plate motions and upper mantle flow can be removed [*Becker*, 2008]. Although relative plate motions are well constrained, we have no direct observations of mantle flow beneath the asthenosphere. Therefore, the contribution of mantle flow to asthenospheric deformation must be inferred from a mantle flow model driven by mantle density heterogeneity. Such models have been used to predict asthenospheric anisotropy in the past [e.g., *Gaboret et al.*, 2003; *Becker et al.*, 2003, 2006a, 2006b; *Behn et al.*, 2004; *Hammond et al.*, 2005; *Conrad et al.*, 2007], but are sensitive to the assumed upper mantle viscosity structure.

[7] Using a global mantle flow model driven by a combination of plate motions and mantle density structure, *Becker* [2008] found that azimuthal anisotropy constrained by surface waves is most consistent with a moderate degree of westward net rotation (1–2 cm/yr on the rotation equator or ~50% of the magnitude associated with the HS3 model). A similar result was recently obtained by *Kreemer* [2009], who used shear wave splitting observations at both oceanic and cratonic locations to constrain net lithosphere rotation about a pole only 4° away from the HS3 pole and at ~50% of the HS3 net rotation rate (Table 1). Unlike *Becker* [2008], *Kreemer* [2009] did not consider the influence of mantle flow on fabric development in the asthenosphere, but instead assumed that asthenospheric LPO always forms parallel to absolute plate motions. While this assumption may be valid beneath fast moving plates (e.g., Pacific basin), previous studies have shown that sub-asthenospheric flow plays an important role in controlling anisotropy when plate velocities are slow (e.g., Atlantic or Indian basins) [e.g., *Behn et al.*, 2004].

[8] In this study, we build upon the results of *Becker* [2008] and *Kreemer* [2009] by jointly constraining both the net lithosphere rotation and the viscosity structure of the upper mantle using independent constraints from surface wave tomography and SKS splitting measurements. To accomplish this, we predict LPO in the asthenosphere using mantle flow models driven by a combination of surface plate motions and tomographically inferred mantle density heterogeneity [e.g., *Behn et al.*, 2004; *Conrad et al.*, 2007]. These flow models include lateral variations in lithospheric thickness and allow us to constrain the viscosity "drop" in the asthenosphere relative to the upper mantle. Using these models, we identify an upper bound on the magnitude of net rotation shear that can be introduced into asthenospheric deformation while satisfying the observed anisotropy. Because the viscosity structure of the upper mantle controls the partitioning of shear between the asthenosphere and underlying mantle, this upper bound suggests an important tradeoff between lithospheric net rotation and asthenospheric viscosity drop.

2. Asthenospheric Anisotropy and Net Rotation

[9] To probe the anisotropic constraint on net rotation and asthenospheric viscosity, it is useful to decompose asthenospheric deformation into components driven separately by mantle flow and absolute plate motions, and by separating the latter component into fields driven by relative plate motions in the NNR frame and by net rotation of the lithosphere (Figure 1). This linear separation into 3 parts can be accomplished if we assume a Newtonian rheology for the mantle and consider asthenospheric deformation away from complexities associated with plate boundaries or localized density heterogeneities (e.g., plumes or convective instability). Beneath a rigid surface plate, mantle flow driven by mantle density heterogeneity generates simple shear within a low-viscosity asthenospheric layer (Figure 1a). Surface plates moving above a passive mantle also generate simple shear within the asthenospheric layer, but generally in a different direction than the shear produced by mantle flow, and with the opposite vertical sense (Figure 1b). When combined, these two flows yield a mantle flow field that is driven simultaneously by surface plate motions and mantle density heterogeneity. *Behn et al.* [2004] noted that the shear strain rate for the density-driven (mantle flow) component of the combined flow field is inversely proportional to the absolute mantle viscosity. By contrast, strain rates for plate-driven flow depend only on the radial (or lateral) variations in viscosity, and not on the absolute viscosity. Thus, the linear combination of these two fields depends primarily on the value chosen for the absolute mantle viscosity, which we define as the viscosity scale factor β following *Behn et al.* [2004] and *Conrad et al.* [2007] (specifically, β expresses the upper mantle viscosity relative to a base value of 10^{21} Pa s). Plate-driven flow dominates for large β (high upper mantle viscosity) because high viscosity tends to damp density-driven flow relative to plate

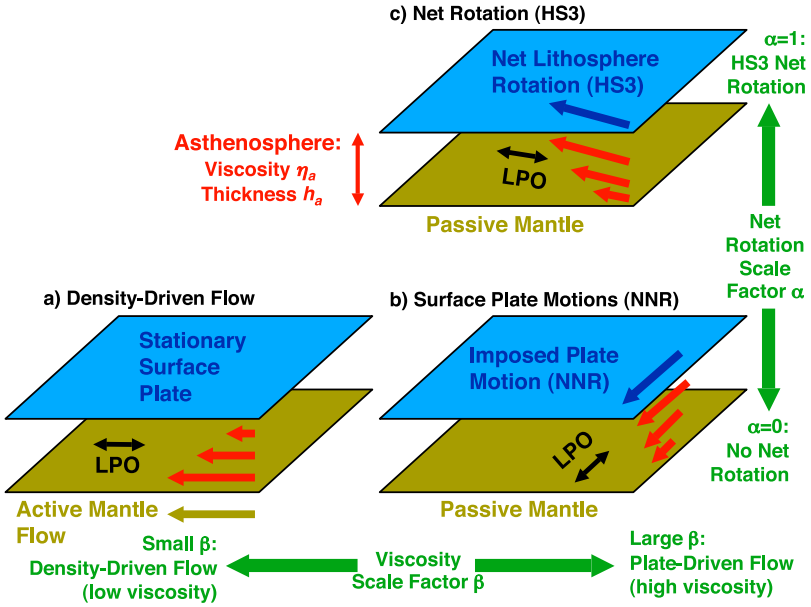

Figure 1. Diagram showing the three end-member flow fields that are combined to produce a global flow model: (a) density-driven flow induced by mantle density heterogeneity, (b) plate-driven flow in the NNR frame, and (c) net rotation–driven flow consistent with HS3 net rotation (Table 1). Linear combinations of these different flow fields are formed by adjusting the scale factors for net rotation (α), viscosity (β), and the drop in viscosity within the asthenosphere relative to the upper mantle (η_a/η_{um}).

motions. The reverse is true for small β (low upper mantle viscosity). By modeling mantle flow in an NNR frame, *Conrad et al.* [2007] constrained $0.3 < \beta < 0.7$, which implies an upper mantle viscosity between 0.3 to 0.7×10^{21} Pa s.

[10] In this study, we introduce net rotation of the lithosphere above a passive mantle (Figure 1c) into the linear combinations of plate-driven and density-driven flow fields. To accomplish this, we impose net rotation consistent with the HS3 model [*Gripp and Gordon*, 2002], but scale the magnitude of the rotation by the dimensionless net rotation scale factor α ranging from 0 (consistent with NNR) to 1 (consistent with HS3). We choose the amplitude-scaled HS3 model to represent the range of possible net rotations because, as discussed above, most other net rotation models produce similarly directed westward lithospheric drift, but with varying magnitudes that are all slower than that of the HS3 model [*Becker*, 2006; *Becker and Faccenna*, 2009] (Table 1). Although the lithosphere moves above a passive mantle, the location of the core-mantle boundary (CMB) must be held fixed to prevent uniform rotation of the entire mantle. Thus, the contribution of lithosphere net rotation to the total mantle flow field is simply the shear flow between the moving lithosphere and the nonrotating CMB. This flow is then distributed within the various intermediate layers of the mantle in proportions that vary inversely with each layer's relative viscosity.

[11] By choosing values for α and β, we can examine a range of relative contributions of density-driven (Figure 1a), plate-driven (Figure 1b), and net rotation–driven (Figure 1c) flow to the global mantle flow field. Because the asthenospheric component of the deformation associated with each of these flow fields depends on the viscosity of the asthenosphere relative to that of the upper mantle, we compute the linear combination of these flow fields for a range of viscosity values for the asthenospheric layer. It is important to remember that the same viscosity structure must be employed for each separate flow field that form the linear combination. To achieve this, we must assume a linear (Newtonian) rheology, which is inconsistent with the non-Newtonian (power law) dislocation creep mechanism that creates anisotropic fabric in the asthenosphere [*Karato and Wu*, 1993]. Thus, our method ignores any viscosity variations induced by the power law rheology, and implicitly assumes that any power law weakening is incorporated into our choice of a Newtonian asthenospheric viscosity. This assumption is valid to first order because NNR plate motions, which induce the fastest asthenospheric flows, likely govern asthenospheric strain rates, and thus effective viscosity. Because the NNR plate motions do not vary between

models, the effective viscosity of the asthenosphere should remain relatively constant between the different cases, and thus can be chosen a priori as we have done here. Furthermore, flow models that incorporate power law rheology into the asthenosphere have shown that it produces only small changes in mantle flow patterns [*Christensen*, 1984; *Cadek et al.*, 1993] and their interaction with plate motions [*Becker* 2006]. Nevertheless, the effect of non-Newtonian rheology on the generation of anisotropic fabric in global mantle flow models is a topic for further study.

[12] The linear combination of flow fields yields a prediction for present-day asthenospheric deformation that can be used to predict LPO in olivine aggregates, and thus the anisotropic fabric in the asthenosphere. To compare this predicted fabric to seismic observations, we calculate the infinite strain axis (ISA), which is the orientation of the long axis of the finite strain ellipsoid after unlimited exposure to a given velocity gradient tensor [*Kaminski and Ribe*, 2002]. Here we are assuming that LPO in the asthenosphere develops quickly; specifically that simple shear rotates the LPO toward the ISA faster than the ISA changes along flow lines. *Kaminski and Ribe* [2002] showed that this assumption can be tested by calculating the grain orientation lag parameter, Π, which is the ratio of these rotation rates. If $\Pi < 0.5$ then the ISA is a valid estimate for the LPO and there is no need to calculate the past strain history of olivine aggregates. The advantage of using the ISA to approximate the LPO is that the ISA and Π can be calculated from an instantaneous flow field and its first time derivative [*Kaminski and Ribe*, 2002]. This greatly simplifies computations and eliminates uncertainty associated with fully time-dependent calculations. *Conrad et al.* [2007] showed that away from plate boundaries, LPO formation in the asthenosphere is sufficiently fast that $\Pi < 0.5$ throughout most of the asthenosphere. Thus, we use the ISA to approximate LPO for the linear combination of flow fields described above, and exclude areas where $\Pi > 0.5$ from our analysis.

3. Models for Global Asthenospheric Flow

[13] We developed global mantle flow models similar to those of *Conrad et al.* [2007], using the finite element code CitcomS [*Zhong et al.*, 2000; *Tan et al.*, 2006] and a grid with 157 km horizontal resolution and vertical resolution varying from 150 km (lower mantle) to 25 km (above 350 km depth). Our viscosity structure consists of a uniform viscosity lower mantle (below 670 km), an asthenosphere (above 300 km and below the lithospheric base), and a lithosphere, with reference viscosities that are 50, 0.03 to 1.0, and up to 1000 times the $\eta_{um} = 10^{21}$ Pa s viscosity of the upper mantle (300–670 km), prior to scaling by β. We perform all calculations for several different values of asthenospheric viscosity within the range $0.03\eta_{um} \leq \eta_a \leq 1.0\eta_{um}$ in order to examine the influence of asthenospheric viscosity on LPO. Following *Conrad et al.* [2007], we introduce a smooth transition from the low-viscosity asthenosphere to the high-viscosity lithosphere, and incorporate lateral viscosity variations above 300 km depth by assigning a variable thickness to the lithosphere that is consistent with seafloor age (for oceans) or near-surface tomography (for continents).

[14] For density-driven flow, we employ rigid surface boundary conditions and free slip conditions at the CMB. We assign densities in the mantle by converting velocity anomalies in the S20RTSb seismic tomography model [*Ritsema et al.*, 2004] to densities using a constant velocity-density conversion factor of 0.15 g cm^{-3} km^{-1} s, which is consistent with both laboratory data [e.g., *Karato and Karki*, 2001] and previous studies [e.g., *Behn et al.*, 2004; *Conrad et al.*, 2007]. Following previous work [e.g., *Lithgow-Bertelloni and Silver*, 1998; *Conrad et al.*, 2007], we do not impose density anomalies above 325 km depth because seismically fast velocity anomalies associated with continental roots have been shown to correspond to neutrally buoyant "tectosphere" [e.g., *Jordan*, 1975] (note that we do use these cratonic velocity anomalies to define lithospheric viscosity variations [e.g., *Conrad and Lithgow-Bertelloni*, 2006]). The resulting density-driven flow (Figure 2a) at the base of the asthenosphere (300 km) exhibits horizontal convergence above downwellings (primarily caused by circum-Pacific and Tethyn subduction), and divergence above upwellings (primarily beneath southern Africa and the Pacific basin). The LPO associated with this flow is approximated using the ISA calculated at the center of the asthenosphere (200 km depth) where shear gradients are greatest. In general, the predicted ISA (Figure 2b) parallels the density-driven flow directions at the base of the asthenosphere (Figure 2a), and the fact that $\Pi < 0.5$ in most locations (Figure 2b) indicates that time advection of strain history is not necessary.

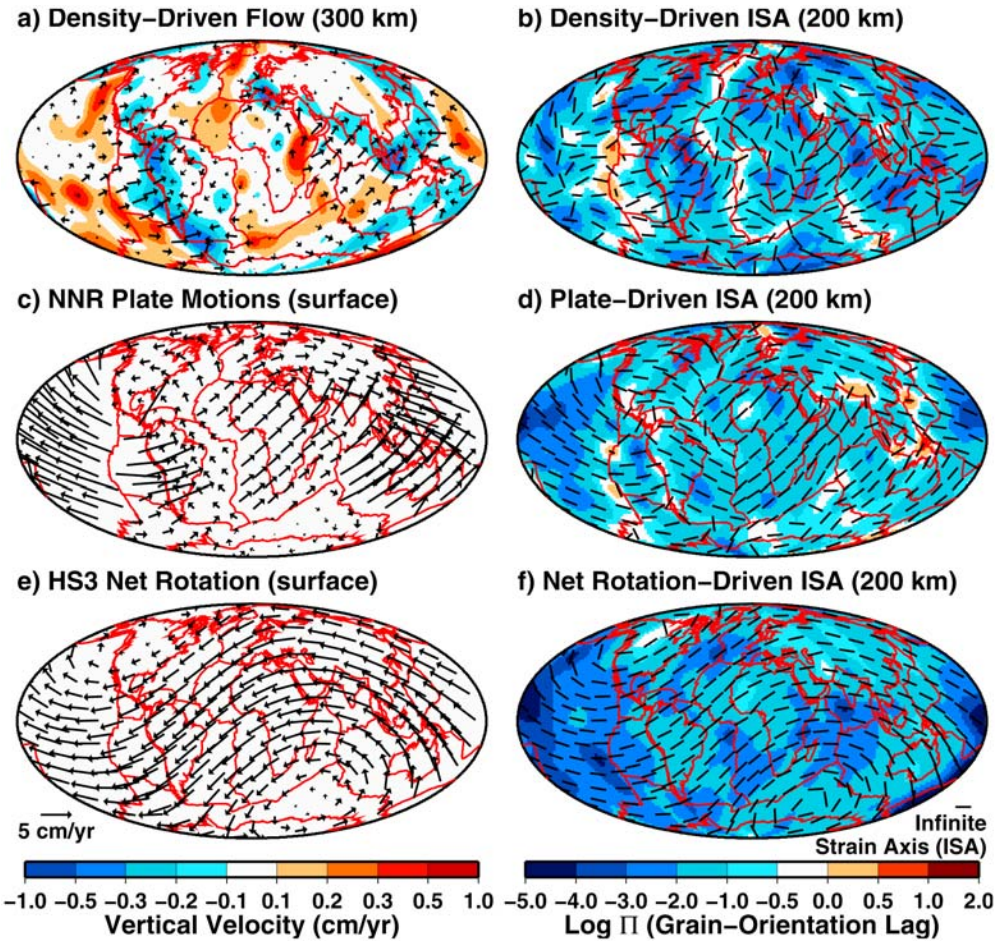

Figure 2. (a, c, and e) Mantle flow velocities and (b, d, and f) ISA and Π predictions for density-driven flow (Figures 2a and 2b), NNR plate-driven flow (Figures 2c and 2d), and HS3 net rotation–driven flow (Figures 2e and 2f). Velocities are shown at the base of the asthenosphere (300 km) for density-driven flow (Figure 2a) and at Earth's surface for plate-driven (Figure 2c) and HS3 net rotation–driven (Figure 2e) flows. ISA and Π (Figures 2b, 2d, and 2f) are shown in the midasthenosphere at 200 km depth, where we compare linear combinations of these model predictions to observations of asthenospheric anisotropy.

[15] For plate-driven flow, we impose NUVEL-1A plate motions [*DeMets et al.*, 1994] for 13 plates in the NNR reference frame as velocity boundary conditions on the surface of the finite element grid (Figure 2c) and free slip conditions at the CMB. The resulting ISA at 200 km depth (Figure 2d) is roughly parallel to plate motions and is a good approximation for anisotropy because $\Pi < 0.5$ except near some major plate boundaries. For net rotation–driven flow, we impose net rotation consistent with the HS3 [*Gripp and Gordon*, 2002] model as a surface velocity boundary condition. If we retain the same free slip conditions on the CMB that we used for the density- and plate-driven flows, we find that the imposition of any net lithosphere rotation simply induces a solid body rotation of the entire mantle over the CMB without inducing any deformation. For example, imposing the full HS3 velocity field (HS3 net rotation and NNR plate motions combined) with a free slip CMB induces the same asthenospheric anisotropy field as NNR plate motions by themselves because the net rotation component induces no deformation. To prevent solid body rotation of the mantle, which is unphysical, we apply a rigid boundary condition at the CMB when computing the net rotation–driven flow. This condition induces shear deformation that is distributed within the various viscous layers of the mantle. When this shearing flow field is combined with the NNR plate-driven flow field (assuming a value for α), the result is a flow field that is driven by surface plate motions that include some net rotation, but with a free slip CMB without any net rotation component. We find that HS3 net

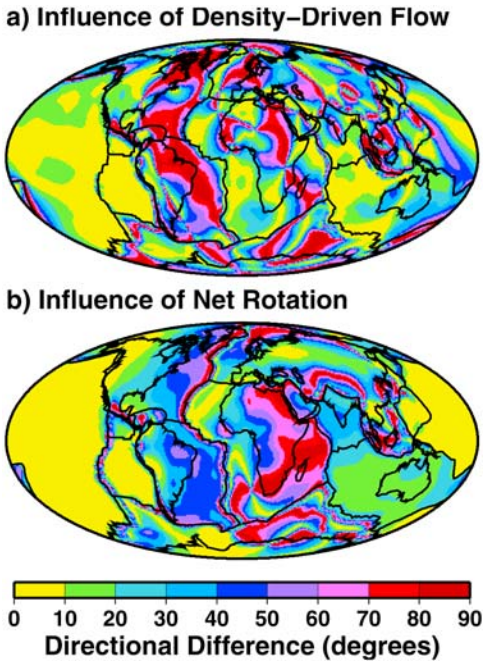

Figure 3. Angular difference between the predicted ISA at 200 km depth for plate-driven flow with no net rotation (Figure 2d) and (a) the combination of plate- and density-driven flow with no net rotation (assuming β = 0.5 as in the work by *Conrad et al.* [2007]) and (b) the combination of plate-driven flow and net rotation HS3 flow (assuming α = 1).

rotation alone induces westward motion of the lithosphere (Figure 2e) that generates a rotation-parallel pattern of ISA in the asthenosphere (Figure 2f). Although Π varies with distance from the rotation pole as well as laterally because lithospheric thickness variations induce perturbations in asthenospheric flow, $\Pi < 0.5$ everywhere.

[16] We generate a combined flow field by summing the velocity fields (both horizontal and vertical components) of the density-driven, plate-driven, and net rotation–driven components after first dividing the density-driven velocities by β and multiplying net rotation–driven velocities by α. The boundary conditions for this combined model are imposed plate motions on the surface and free slip at the CMB with the important condition that any CMB net rotation has been removed and is instead distributed as shear deformation within the mantle's viscous layers. Because we are using a linear viscosity law, we can form linear combinations (Figure 1) of density-driven (Figure 2a), plate-driven (Figure 2c), and rotation-driven flow fields (Figure 2e) that we compute separately for each asthenospheric viscosity structure. Using these combined flow fields, we then compute Π and the 3-D orientation of the ISA globally (note that we cannot form linear combinations of the Π and ISA fields (e.g., Figures 2b, 2d, and 2f) because these quantities do not sum linearly in the way the flow fields do).

[17] To assess which regions of the globe are most sensitive to variations in β and α, we compared the ISA orientations from plate-driven flow alone ($\alpha = 0$ and $\beta \rightarrow \infty$) to plate- and density-driven flows combined (α = 0 and β = 0.5 (Figure 3a)) and to plate-driven flow assuming the HS3 net rotation (α = 1 and $\beta \rightarrow \infty$ (Figure 3b)). We find that the inclusion of density-driven flow rotates the ISA significantly across many continental locations and in parts of the Atlantic and Indian ocean basins. However, the Pacific is relatively insensitive to the introduction of density-driven flow (Figure 3a) because plate motions there are much faster than mantle flow velocities at the base of the asthenosphere. Thus, plate-driven flow dominates the formation of LPO in the Pacific regardless of the underlying mantle flow field (Figures 2a–2d). The effects of density-driven flow, however, are much more pronounced outside of the Pacific basin (Figure 3a) where surface plate motions are slower [*Conrad et al.*, 2007]. Similarly, sublithospheric anisotropy in the Pacific is relatively insensitive to the introduction of HS3 net rotation (Figure 3b) because the HS3 net rotation is generally parallel to Pacific plate motions and therefore does not change the underlying anisotropic fabric (Figures 2c–2f). The ISA beneath plates outside of the Pacific basin, however, is significantly affected by the introduction of net rotation (Figure 3b). Thus, we expect stronger constraints on both upper mantle viscosity and net rotation to come from anisotropy observations in the Atlantic and Indian basins, rather than from the Pacific basin.

4. Comparison to Anisotropy Observations

[18] Previous studies have used azimuthal anisotropy to constrain either the net rotation of the lithosphere [e.g., *Becker*, 2008] or the absolute mantle viscosity [e.g., *Behn et al.*, 2004; *Conrad et al.*, 2007] individually, but not jointly. Here, we use azimuthal anisotropy to simultaneously constrain three free parameters: (1) the net rotation scaling parameter α; (2) the viscosity scaling parameter β; and (3) the decrease in viscosity between the asthenosphere and the upper mantle, η_a/η_{um}. We do this by systematically varying α

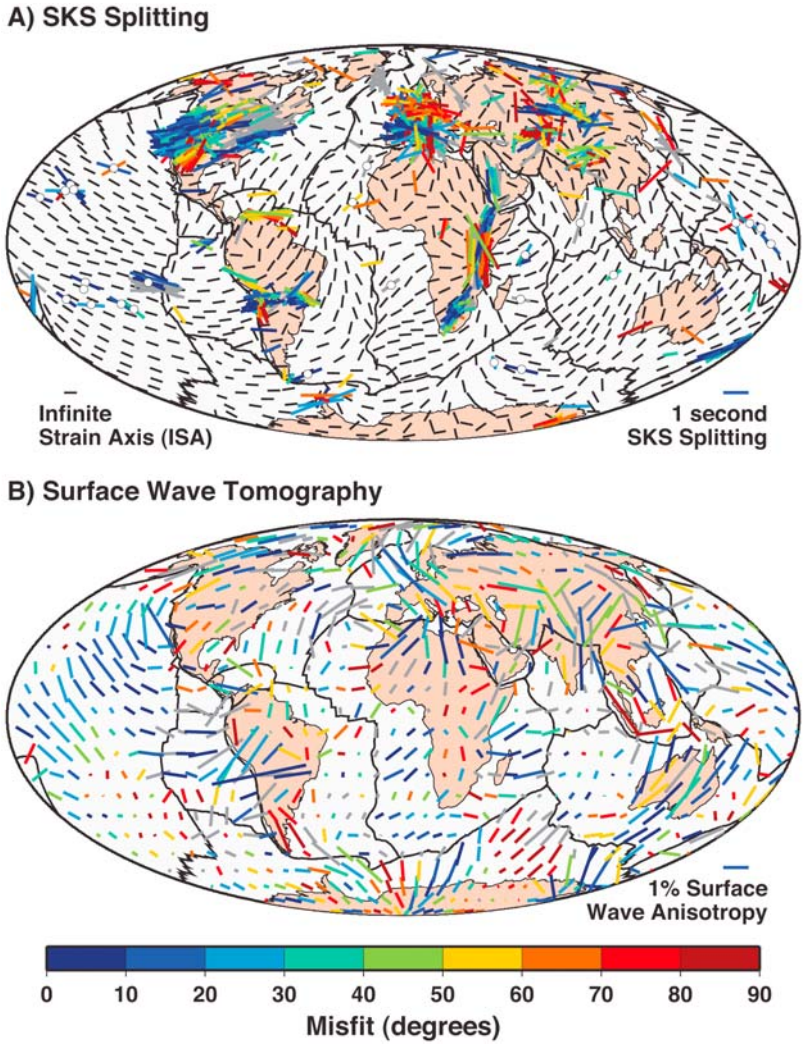

Figure 4. Misfit between the predicted ISA orientations (black bars in Figure 4a) at 200 km depth for $\beta = 0.5$, $\alpha = 0.2$, and $\eta_a = 0.1\eta_{um}$ with (a) the global SKS data compilation described in section 4.1 and (b) the *Debayle et al.* [2005] surface wave anisotropy model. Misfit in both cases is expressed in degrees using colors, where gray indicates regions where misfit is not included in global averages because $\Pi > 0.5$. The length of colored bars indicates the amplitude of anisotropy, seconds for SKS in Figure 4a and % anisotropy for surface waves in Figure 4b. The 26 midplate oceanic SKS stations that are used to compute average misfit for this flow field are denoted with open circles in Figure 4a.

between 0 (NNR) and 1 (HS3 net rotation) and β between 0.01 (density-driven flow dominates) and 10 (plate-driven flow dominates) for four different η_a/η_{um} ratios: $\eta_a = 0.03\eta_{um}$ (lowest viscosity asthenosphere), $\eta_a = 0.1\eta_{um}$, $\eta_a = 0.3\eta_{um}$, and $\eta_a = \eta_{um}$ (no viscosity drop). We then compute the ISA and Π from the combined flow field, and compare the orientation of predicted ISA (for locations more than 500 km from plate boundaries and where $\Pi < 0.5$) to observations of azimuthal anisotropy. To evaluate each linear combination, we compute the average misfit as the average angular difference between the predicted ISA and the anisotropy observation (SKS or surface wave tomography model). Minimization of this misfit measure provides constraints on α, β, and η_a/η_{um}.

4.1. Global SKS Splitting Data

[19] We compared predicted ISA orientations to the SKS splitting database that was used by *Conrad et al.* [2007], which contains ~1350 splitting measurements from 87 studies compiled in the Arizona State University Global Upper Mantle Anisotropy Data set (http://geophysics.asu.edu/anisotropy/upper) and several recent shear wave splitting studies in

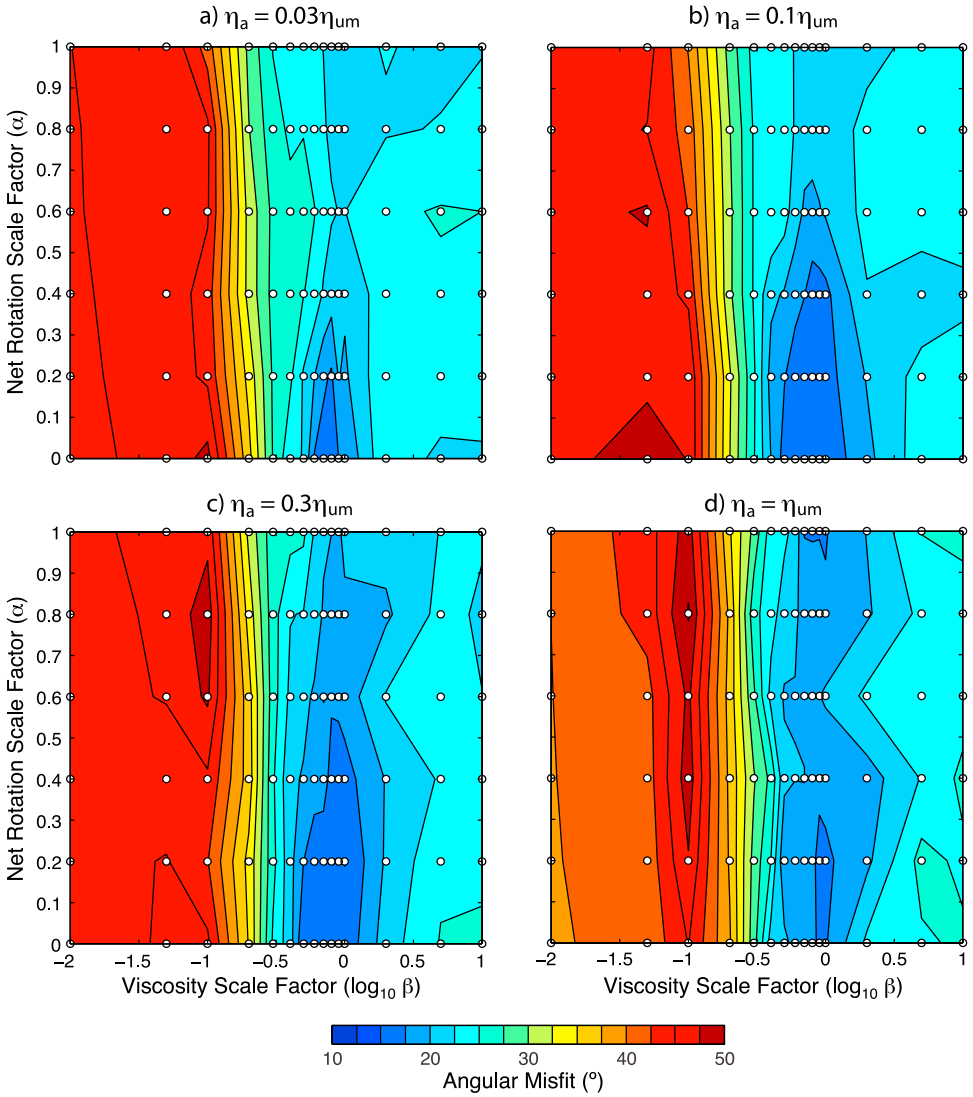

Figure 5. Average misfit between model predictions at 200 km depth and SKS oceanic splitting data as a function of net rotation (expressed by α) and mantle viscosity (expressed by β) for four different values of the asthenospheric viscosity drop (η_a/η_{um}). Excluded from this average are stations within 500 km of a plate boundary and locations where $\Pi < 0.5$.

the ocean basins [*Wolfe and Silver*, 1998; *Smith et al.*, 2001; *Klosko et al.*, 2001; *Fontaine et al.*, 2005; *Hammond et al.*, 2005]. In general, these data (Figure 4a) are located primarily in continental areas, where the presence of fossil anisotropy in the lithosphere, which cannot be predicted by flow models, may complicate a comparison to flow-induced ISA orientations [e.g., *Fouch and Rondenay*, 2006; *Conrad et al.*, 2007; *Becker et al.*, 2008]. To avoid this lithospheric fabric, we first examined comparisons to the 106 oceanic stations within the database, where lithospheric fossil fabric is expected to be minimal [e.g., *Behn et al.*, 2004]. Of these oceanic stations, we eliminated those that are located within 500 km of a plate boundary, as our mantle flow model does not have sufficient resolution to predict ISA and Π accurately in these regions [*Conrad et al.*, 2007]. This leaves 26 midplate oceanic stations for which we have SKS splitting data that can reliably be used to constrain our flow models.

[20] For each flow model (consisting of choices for α, β, and η_a/η_{um}), we compare predictions for ISA at 200 km depth (the approximate center of the asthenosphere) for each of the 26 midplate ocean SKS stations (e.g., Figure 4a). We then excluded stations where $\Pi > 0.5$ because ISA may not accurately predict LPO at these locations, and

compute the average misfit between the SKS and ISA orientations at the remaining stations. This typically results in >20 "clean" stations (the precise number varies because Π depends on α and β) at which the misfit is calculated (Figure 4a). The average misfit (Figure 5) shows similar patterns among the 4 models for asthenospheric viscosity. In general, we find high average misfit for flow fields dominated by density-driven flow ($\beta < 0.3$). Plate-driven flow (large β) results in a lower misfit than density-driven flow, however, the minimum misfit is found for values of β in an intermediate range of $0.4 < \beta < 1.5$ (Figure 5). This range is relatively insensitive to asthenospheric viscosity, η_a, and net rotation, α, and is very similar to the range in β reported by *Conrad et al.* [2007], who assumed the NNR frame ($\alpha = 0$). This range should be sensitive, however, to the viscosity contrast between the upper and lower mantle ($\eta_{lm}/\eta_{um} = 50$) and the conversion factor we used to assign densities to seismic velocity anomalies (0.15 g cm^{-3} km^{-1} s). Decreasing the former or increasing the latter will tend to enhance density-driven flow, which would shift the misfit values in Figure 5 to the right toward larger values of β. Therefore, our constraints on the range of β could shift toward higher (or lower) upper mantle viscosities for either relatively weaker (or stronger) lower mantle or for larger (or smaller) amplitudes of mantle density heterogeneity than we have assumed here.

[21] The SKS constraint on net rotation (α) is weaker than the constraint on absolute viscosity (β), with a minimum misfit generally occurring over a broad range of values for α (Figure 5). The permitted range of α, however exhibits a stronger dependence on the asthenospheric viscosity η_a than does β. Overall, the SKS data are best fit with a small net rotation for low asthenospheric viscosities (e.g., $\alpha < 0.2$ for $\eta_a = 0.03\eta_{um}$ (Figure 5a)), and greater net rotation is permitted as asthenospheric viscosity increases (e.g., $\alpha < 0.55$ for $\eta_a = 0.3\eta_{um}$ (Figure 5c)). For no drop in asthenospheric viscosity relative to the upper mantle ($\eta_a = \eta_{um}$), the SKS data provide very little constraint on α (Figure 5d). Because most of the net rotation is accommodated within the asthenosphere and upper mantle, rather than within the higher-viscosity lower mantle, we expect these constraints on α to be relatively insensitive to our choice of lower mantle viscosity, as long as the lower mantle remains significantly more viscous than the upper mantle. Similarly, our constraints on α and β should be relatively insensitive to the asthenospheric thickness (nominally about 200 km). This is because a thicker or thinner asthenosphere will change the amplitudes of each asthenospheric shear component equally and thus will not affect their relative amplitudes, which are controlled by α and β.

[22] The tighter net rotation constraint for smaller asthenospheric viscosity drops implies that the SKS data permit a maximum amount of shear associated with net rotation to be accommodated in the asthenosphere. For a low-viscosity asthenosphere, most of the relative motion between the lithosphere and the deep mantle is accommodated within the asthenosphere, because its low viscosities make it easier to deform. Thus for $\eta_a = 0.03\eta_{um}$, only ~20% of the HS3 net rotation can be included to obtain a best fit for the SKS data (Figure 5a). If the asthenospheric viscosity is increased to $\eta_a = 0.1\eta_{um}$, more of the net rotation shear will be accommodated within the nonasthenospheric mantle, and the portion that remains within the asthenosphere will not produce as strong an anisotropic fabric. In this case, larger net lithosphere rotations are permitted (up to about 45% of HS3) before the fit to SKS observations significantly degrades (Figure 5b). Finally, without an asthenospheric viscosity drop ($\eta_a = \eta_{um}$), the entire upper mantle accommodates net rotation shear and asthenospheric anisotropy does not constrain the amplitude of net rotation.

[23] In summary, the oceanic SKS data constrain β to be in the range of $0.4 < \beta < 1.5$, and $\alpha < 0.5$ for asthenospheric viscosity drops of about an order of magnitude. These values are consistent with earlier estimates of β by *Conrad et al.* [2007] using the same SKS data, and α by both *Becker et al.* [2008] using the surface wave model of *Ekström* [2001] and *Kreemer* [2009] using SKS data. The average angular misfit between the oceanic SKS data and the ISA predictions from the best fitting flow model is less than 15°, and thus within the nominal uncertainty of the splitting observations [*Behn et al.*, 2004]. This average misfit is also smaller than the minimum misfit of 19° that *Kreemer* [2009] obtained by using a similar set of oceanic SKS data. We note that *Kreemer*'s [2009] study allowed for a full range of variation in the net rotation parameter α and the net rotation axis, but did not consider density-driven flow and therefore implicitly considered only the limit of large β. The *Kreemer* [2009] study therefore may have detected a local minimum that is also present in our study (at $\log_{10}(\beta) = 1.0$, $\alpha = 0.4$, and $\eta_a = 0.1\eta_{um}$ in Figure 5b), but not the global minimum, which requires a component of density-driven flow (smaller β). We find that models producing best fits

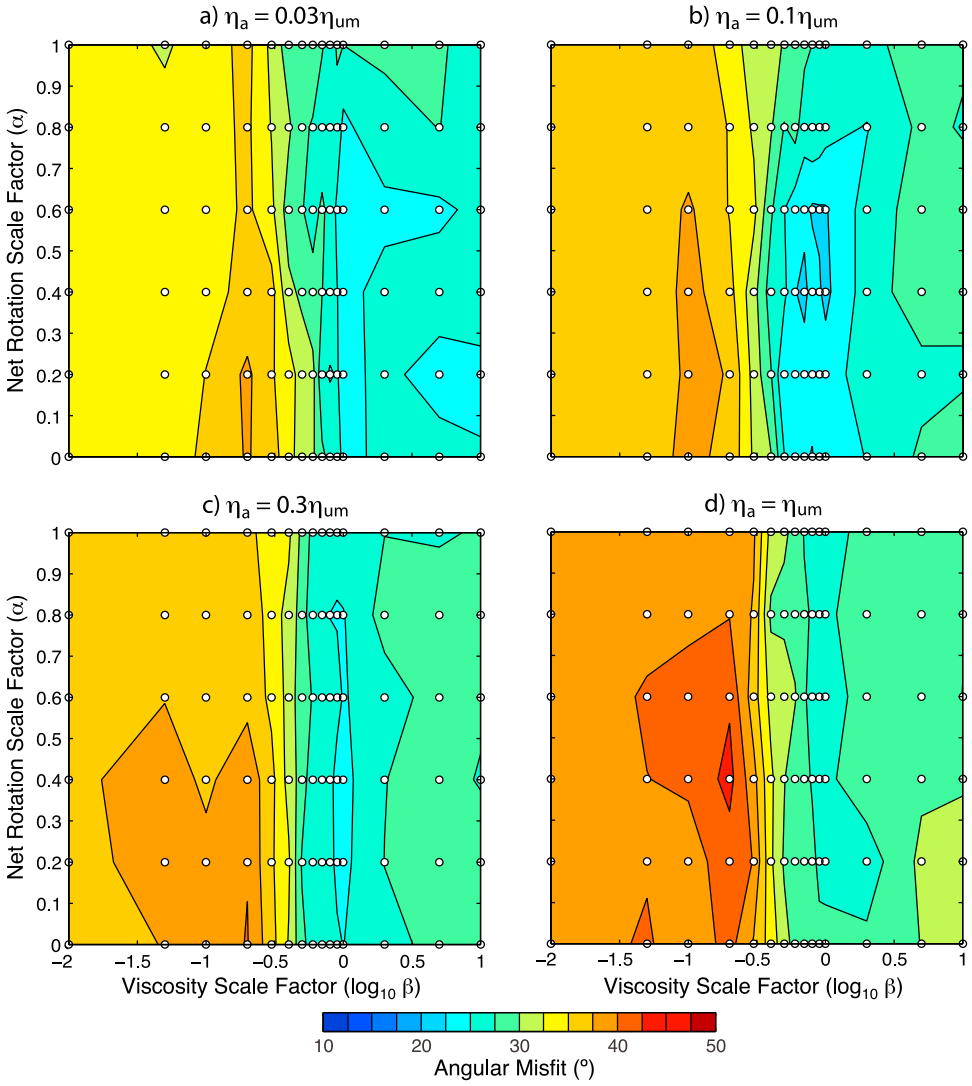

Figure 6. Average angular misfit between model predictions and *Debayle et al.* [2005] surface wave data at 200 km depth beneath oceanic areas for four different values for the asthenospheric viscosity drop (η_a/η_{um}). Excluded from this average are oceanic data where the amplitude of anisotropy is less than 25% of the maximum amplitude of anisotropy and locations where $\Pi < 0.5$.

to the anisotropy (as we show on an intermediate model using $\beta = 0.5$, $\alpha = 0.2$, and $\eta_a = 0.1\eta_{um}$ in Figure 4) do a good job of fitting ocean island SKS observations in the Pacific, where they are dominated by Pacific plate motion, but also in the Atlantic and Indian basins, where flow driven by a combination of plate motions and mantle density heterogeneity is required to match the SKS observations [*Behn et al.*, 2004].

4.2. Surface Wave Tomography

[24] To test our flow models against a second anisotropy data set that is independent of both the SKS data and the *Ekström* [2001] surface wave model utilized by *Becker* [2008], we examined azimuthal anisotropy derived from the surface wave model of *Debayle et al.* [2005] (Figure 4b). Average angular misfits were computed between the ISA and azimuthal anisotropy at 200 km depth throughout the ocean basins. Because surface wave models provide greater lateral smoothing compared to SKS data, we expect regions with the largest amplitude anisotropy to produce the strongest constraints on the flow models. Therefore, following *Becker et al.* [2003], we exclude regions of the oceans where the amplitude of azimuthal anisotropy in the *Debayle et al.* [2005] model is less than 25% of the maximum amplitude of

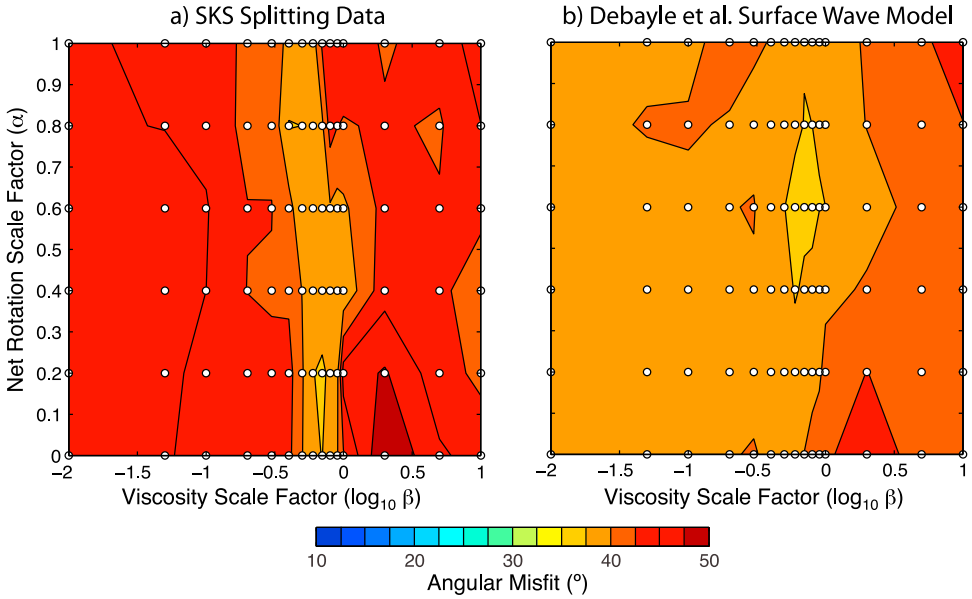

Figure 7. Average angular misfit at 200 km beneath continental regions (assuming $\eta_a = 0.1\eta_{um}$), as a function of α and β for (a) the SKS splitting data as in Figure 5b and (b) the filtered *Debayle et al.* [2005] surface wave model as in Figure 6b.

anisotropy. In addition, as discussed above we exclude regions where $\Pi > 0.5$.

[25] The surface wave data provide similar constraints on β, α, and η_a/η_{um} (Figure 6) to those derived from the SKS data (Figure 5), although the SKS data feature a smaller average angular misfit. This may be the result of lateral smoothing and/or inversion uncertainty associated with the *Debayle et al.* [2005] model. Nevertheless, we find a best fitting region within the range of $0.5 < \beta < 2$ (Figure 6), which is similar to the range found for the SKS data (Figure 5), and very poor fits for $\beta <$ 0.3 where density-driven flow dominates. Comparisons at shallower (175 km) and deeper (225) depths in the asthenosphere produce similar results, with the 175 km and 225 km depths providing slightly weaker constraints on β and α, respectively.

[26] The surface wave constraint on net rotation is poorer than it is for the SKS data, although we do find best fits for net rotation between 40 and 60% of the HS3 net rotation when $\eta_a = 0.1\eta_{um}$ (Figure 6b), which is similar to the upper bound of the SKS constraint (Figure 5b). The absence of a low-viscosity asthenosphere (Figure 6d) produces a poorer fit to the surface wave model, as we found for the SKS data (Figure 5d). Thus, the same flow models that provide the best fits to SKS observations also produce the best fits to the *Debayle et al.* [2005] model. A closer examination of misfits for one such model (e.g., $\beta = 0.5$, $\alpha = 0.2$, and $\eta_a = 0.1\eta_{um}$ (Figure 4b)) shows that large amplitude anisotropy in the Pacific, Atlantic, and Indian basins is generally well predicted by the ISA orientations (longest bars in Figure 4b), while regions of smaller amplitude anisotropy generally show a poorer fit.

4.3. Continental Anisotropy

[27] Continental anisotropy has been attributed to both fossil fabric preserved within old cratonic lithosphere [*Silver and Chan*, 1988; *Silver et al.*, 2004] as well as lithospheric deformation associated with recent or ongoing orogenic events [*Silver*, 1996; *Flesch et al.*, 2005]. Because our models of asthenospheric shear flow cannot predict anisotropic fabric in either cratonic or actively deforming lithosphere, we do not expect our ISA predictions to match observations of anisotropy in continental areas with strong preexisting mantle fabric [*Conrad et al.*, 2007]. In fact, we find that our fit to continental anisotropy is significantly poorer than it is for oceanic anisotropy for all values of α, β, and η_a/η_{um}; both for the SKS data (Figure 7a) and for the *Debayle et al.* [2005] surface wave model (Figure 7b). Nevertheless, we do find a slight improvement in the average continental misfit for $0.5 < \beta < 1.0$ (Figure 7), which is approximately the same mantle viscosity scale factor that we found best fits the oceanic anisotropy data (Figures 5 and 6). This suggests that flow-

induced anisotropy beneath the lithosphere contributes to the net anisotropy in some continental regions, which is consistent with *Kreemer*'s [2009] detection of only 24° misfit between that cratonic SKS observations and plate motions expressed in a best fitting reference frame. For continental anisotropy, the model fit to the surface wave anisotropy (Figure 7b) is slightly better than the fits to SKS splitting data (Figure 7a). This may be because the surface wave model offers some depth resolution, permitting us to more accurately constrain asthenospheric fabric when it lies beneath a layer of lithospheric anisotropy with a different orientation. In contrast, SKS splitting measurements provide an integration of anisotropy in the upper mantle, and therefore will only uniquely constrain asthenospheric fabric in regions where the overlying lithospheric fabric is significantly weaker. One such region may be in western North America, where asthenospheric shear is strongly oriented in an east-west direction [*Silver and Holt*, 2002; *Becker et al.*, 2006b] and matches both SKS observations (Figure 4a) and the *Debayle et al.* [2005] model (Figure 4b).

5. Discussion and Conclusions

[28] Using two independent measures of global asthenospheric anisotropy, we have simultaneously constrained the relative contributions of plate motions, mantle density heterogeneity, and net lithosphere rotation to the global mantle flow field (Figure 8). We find that mantle flow driven by a combination of both plate motions and mantle density heterogeneity is required to predict asthenospheric anisotropy in oceanic areas, particularly within the Atlantic and Indian basins where speeds of surface plates and mantle flow are comparable [e.g., *Behn et al.*, 2004; *Conrad et al.*, 2007]. To obtain an appropriate balance between plate-driven and density-driven flow fields, upper mantle viscosity must be within the range $0.5–1.0 \times 10^{21}$ Pa s, which compares favorably to independent estimates made using constraints from postglacial rebound [e.g., *Mitrovica*, 1996] and sedimentological constraints on deflections of the Earth's surface by mantle flow [e.g., *Spasojevic et al.*, 2009].

[29] Azimuthal anisotropy also places an upper bound on the net rotation of the lithosphere relative to the deep mantle. We find that this upper bound depends on the viscosity drop within the asthenosphere. If the asthenosphere is an order of magnitude less viscous than the underlying mantle, a global net rotation of up to about 0.26°/Myr is permitted (60% of HS3 net rotation (Table 1)), corresponding to a maximum of ~3 cm/yr of westward drift. This suggests that the HS3 model [*Gripp and Gordon*, 2002] overpredicts westward motion, possibly because the Pacific hot spots that primarily define the HS3 reference frame may themselves be drifting eastward at rates of a few cm/yr. As discussed below, this eastward drift of Pacific hot spots may result from eastward directed return flow from Pacific plate motion occurring in the deep mantle beneath the western and central Pacific basin (Figure 8, western portions of sections A–B and C–D and eastern portion of section G–H), which pushes plume conduits eastward [e.g., *Steinberger et al.*, 2004; *Tarduno et al.*, 2009]. By contrast, the plume conduits responsible for the Indo-Atlantic hot spots rise through a more sluggish and less uniform mantle flow field (Figure 8, section E–F) that results from slower Indo-Atlantic plate motions moving in multiple directions as compared to the Pacific basin. Indeed, paleomagnetic data suggest only small motions of Indo-Atlantic hot spots during the past 80 Myr [*Doubrovine and Tarduno*, 2008]. Thus, reference frames based on Indo-Atlantic hot spots [e.g., *O'Neill et al.*, 2005] suggest relatively slow net rotation of ~0.19°/Myr, which corresponds to only ~2 cm/yr of westward drift (~40% of HS3 net rotation (Table 1)) and satisfies the anisotropy constraints. In support of the Indo-Atlantic hot spot frame, *Schellart et al.* [2008] found that this frame minimizes viscous dissipation associated with slab and trench migration compared to other references frames. Other recent studies constrain even slower net rotation, which also satisfies the anisotropy constraint. For example, *van der Meer et al.* [2010] used the deep mantle locations of old subducted material to estimate ~18° of net rotation since the early Cretaceous, which implies a lithospheric drift rate of ~0.12°/Myr. This long-term rotation rate is comparable to net rotation during the 0–5 Ma stage of *Torsvik et al.*'s [2010] recent global plate motion compilation based on global hot spots linked via a mantle flow model (Table 1), and is about 25% of the HS3 net rotation.

[30] Although azimuthal anisotropy constrains net rotation to be less than ~0.26°/Myr (60% of the HS3 net rotation), consistent with a frame based on Indo-Atlantic hot spots, anisotropy observations within the Pacific basin contribute little to this constraint (Figure 3b). By contrast, constraints on net rotation that are obtained from the Pacific basin, such as lithospheric motion relative to Pacific hot spots, suggest faster net rotation (~0.44°/Myr) of

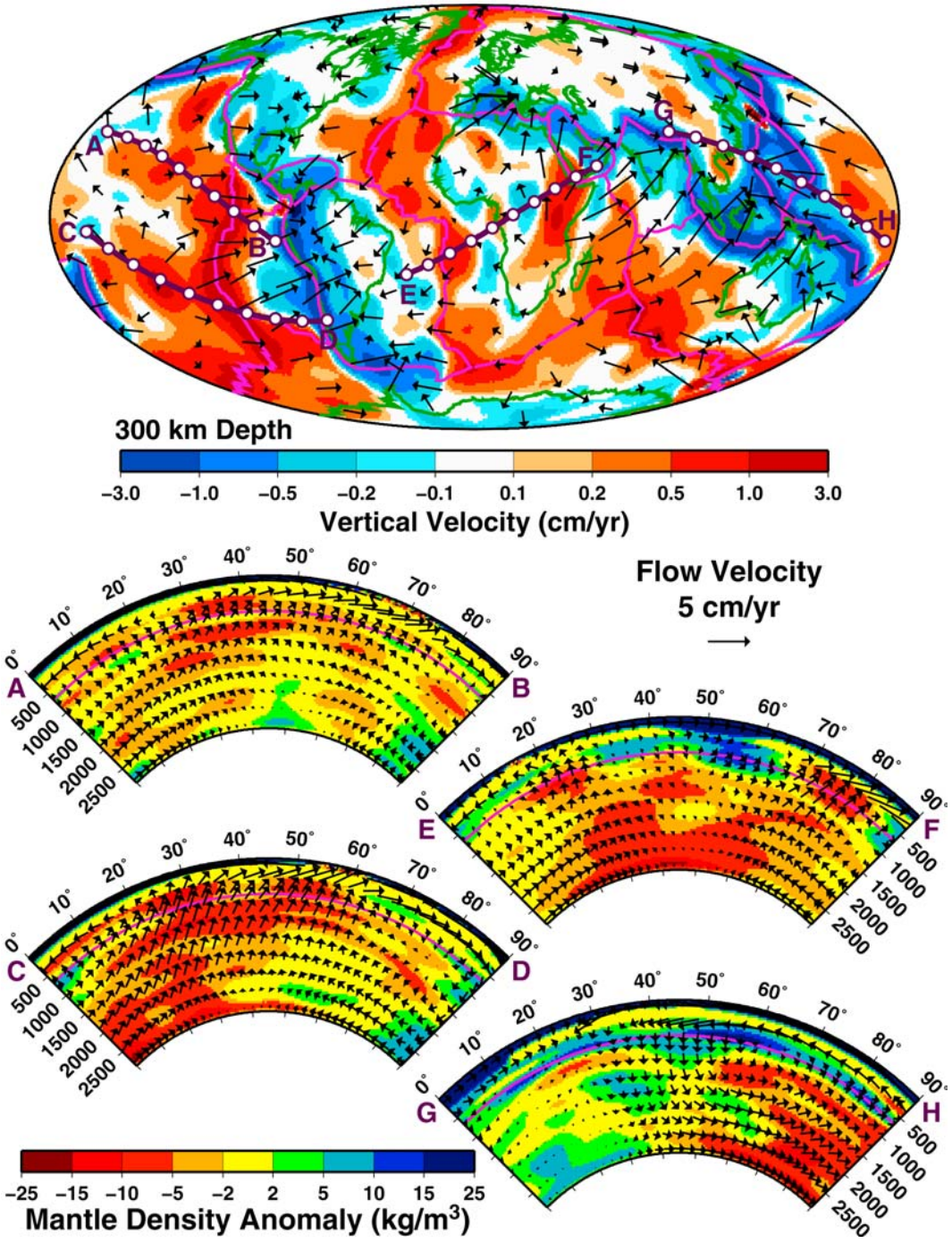

Figure 8. Preferred mantle flow field model constrained by observations of seismic anisotropy in the asthenosphere (a combination of density-driven, NNR plate motion–driven, and net rotation–driven flows assuming $\beta = 0.5$, $\alpha = 0.2$, and $\eta_a = 0.1\eta_{um}$). (top) Map view showing vertical (colors) and horizontal (arrows) flow directions in the midasthenosphere at 300 km depth. (bottom) Profiles showing the flow field (arrows) and the driving mantle density anomaly (colors) along cross sections (locations denoted in Figure 8 (top)).

the HS3 model [*Gripp and Gordon*, 2002]. Our combined flow model (e.g., Figure 8, with a net rotation of 20% of HS3) may help to reconcile this discrepancy between constraints from the Indo-Atlantic and Pacific hemispheres. In particular, the rapid westward motion of the HS3 frame may be useful for interpreting features of the Pacific basin that are tied to the eastward moving deep Pacific mantle, such as the Pacific hot spots. For example, *Long and Silver* [2009] found that the magnitude of

trench-parallel shear wave splitting associated with mantle flow beneath Pacific slabs correlates with the magnitude of trench migration in the HS3 frame. This observation can be explained if trench-parallel flow results from trench migration relative to the deep eastward moving Pacific lower mantle. Correlations of other subduction zone characteristics, such as back-arc stresses [*Heuret and Lallemand*, 2005], slab dip angles [*Lallemand et al.*, 2005], and subducting plate velocity [*Funiciello et al.*, 2008; *Lallemand et al.*, 2008], to the westward motions of trenches in the HS3 frame may also represent an expression of trench motions relative to the deep mantle in which circum-Pacific slabs are anchored [*Husson et al.*, 2008]. Thus, the HS3 frame may express net rotation relative to the mantle deep beneath the Pacific plate, which is moving eastward by a few cm/yr compared to the deep mantle as a whole (Figure 8). In this case, HS3 may be appropriate for expressing the dynamics of the Pacific realm, such as the motions of Pacific trenches and hot spots on the Pacific plate. When expressed relative to the average deep mantle, however, net rotation must be slower than indicated by the HS3 frame, and is consistent with the Indo-Atlantic hot spots (and possibly even eastern Pacific hot spots, as discussed by *Steinberger* [2002]) and the anisotropy constraints discussed here.

[31] Shear deformation associated with net rotation becomes more concentrated within the asthenosphere as asthenospheric viscosity decreases. This results in an enhancement of anisotropic fabric oriented parallel to the imposed net rotation (Figure 2f). Because the anisotropy data place an upper limit on the magnitude of this net rotation fabric, we can alternatively use constraints on net rotation to place bounds on the magnitude of the asthenospheric viscosity drop (i.e., η_a/η_{um}) beneath oceans, which is otherwise difficult to constrain [e.g., *Paulson et al.*, 2007]. For example, we find that net rotation must be less than 20% of HS3 to be consistent with anisotropy constraints if the asthenosphere is 30 times less viscous than the upper mantle. This would require less than 1 cm/yr of maximum drift, which is smaller than inferred using any of the hot spot reference frames listed in Table 1. Therefore, these hot spot reference frames are more consistent with an asthenospheric viscosity drop of 10 than they are with a drop of 30.

[32] It is of course possible that the asthenospheric viscosity drop varies laterally or depends on the amplitude of asthenospheric shear, as we would expect if asthenospheric rheology is non-Newtonian. In these cases, the interaction between asthenospheric shear induced by mantle flow, plate motions, and net rotation would become significantly more complicated than the linear treatment we assume here. Furthermore, it is possible that complexities to asthenospheric flows such as small-scale convection or lithospheric "drips" could interfere with fabric development in some regions. In fact, *van Hunen and Cadek* [2009] showed that the amplitude of azimuthal anisotropy in the asthenosphere is significantly reduced by small-scale convection when measured in an average sense over large regions, as it is in surface wave studies. This may explain why we find poorer fits to the surface wave model of *Debayle et al.* [2005] than we do to the SKS data, many of which may happen to sample asthenosphere that is unaffected by small-scale convection. Other complications, such as the uneven geographic distribution of SKS stations (Figure 4a) and their poor depth resolution, and the potential for lateral and vertical uncertainty in the *Debayle et al.* [2005] anisotropy model, may complicate our comparison of model predictions to anisotropic constraints. Finally, depth variations in our predictions of anisotropy, as well as uncertainty in various model parameters such as lithospheric thickness and mantle viscosity structure, could reduce our ability to use mantle flow models to accurately calculate anisotropic fabric.

[33] Nevertheless, the fact that two independent measures of anisotropic fabric, namely a global database of SKS observations and the *Debayle et al.* [2005] surface wave model, yield similar constraints on our global flow models is extremely encouraging. Furthermore, the result that net lithosphere rotation rate should be less than half that of HS3 is consistent with *Becker* [2008], who reached a similar conclusion using a different global mantle flow model and a different surface wave tomography model, and with *Kreemer* [2009], who used SKS observations and did not consider global mantle flow. Given the consistency of these results, we conclude that asthenospheric anisotropy provides a robust constraint on the relative contributions of mantle density heterogeneity, relative plate motions, and net lithosphere rotation to the global mantle flow field (Figure 8). In particular, anisotropy observations constrain the lithosphere's net rotation relative to the deep mantle (<0.26°/Myr, or 60% of HS3 net rotation), and the absolute viscosities of the upper mantle ($0.5–1 \times 10^{21}$ Pa s) and asthenosphere ($0.5–1 \times 10^{20}$ Pa s).

Acknowledgments

[34] We thank the late Paul G. Silver for enthusiastic and insightful discussions that helped motivate and improve this work, as well as C. Kreemer, B. Steinberger, S. Zhong, an anonymous reviewer, and Editor J. Tarduno for thoughtful and helpful reviews. This research was supported by NSF grants EAR-0855546 (C.P.C.) and EAR-0854673 (M.D.B.).

References

Argus, D. F., and R. G. Gordon (1991), No-net-rotation model of current plate velocities incorporating plate motion model NUVEL-1, *Geophys. Res. Lett.*, *18*, 2039–2042, doi:10.1029/91GL01532.

Becker, T. W. (2006), On the effect of temperature and strain-rate dependent viscosity on global mantle flow, net rotation, and plate-driving forces, *Geophys. J. Int.*, *167*, 943–957, doi:10.1111/j.1365-246X.2006.03172.x.

Becker, T. W. (2008), Azimuthal seismic anisotropy constrains net rotation of the lithosphere, *Geophys. Res. Lett.*, *35*, L05303, doi:10.1029/2007GL032928.

Becker, T. W., and C. Faccenna (2009), A review of the role of subduction dynamics for regional and global plate motions, in *Subduction Zone Geodynamics*, edited by S. Lallemand and F. Funiciello, pp. 3–34, doi:10.1007/978-3-540-87974-9_1, Springer, Berlin.

Becker, T. W., J. B. Kellogg, G. Ekström, and R. J. O'Connell (2003), Comparison of azimuthal seismic anisotropy from surface waves and finite strain from global mantle-circulation models, *Geophys. J. Int.*, *155*, 696–714, doi:10.1046/j.1365-246X.2003.02085.x.

Becker, T. W., S. Chevrot, V. Schulte-Pelkum, and D. K. Blackman (2006a), Statistical properties of seismic anisotropy predicted by upper mantle geodynamic models, *J. Geophys. Res.*, *111*, B08309, doi:10.1029/2005JB004095.

Becker, T. W., V. Schulte-Pelkum, D. K. Blackman, J. B. Kellogg, and R. J. O'Connell (2006b), Mantle flow under the western United States from shear wave splitting, *Earth Planet. Sci. Lett.*, *247*, 235–251, doi:10.1016/j.epsl.2006.05.010.

Becker, T. W., B. Kustowski, and G. Ekström (2008), Radial seismic anisotropy as a constraint for upper mantle rheology, *Earth Planet. Sci. Lett.*, *267*, 213–227, doi:10.1016/j.epsl.2007.11.038.

Behn, M. D., C. P. Conrad, and P. G. Silver (2004), Detection of upper mantle flow associated with the African Superplume, *Earth Planet. Sci. Lett.*, *224*, 259–274, doi:10.1016/j.epsl.2004.05.026.

Burke, K., and J. T. Wilson (1972), Is the African plate stationary?, *Nature*, *239*, 387–390, doi:10.1038/239387b0.

Cadek, O., Y. Ricard, Z. Martinec, and C. Matyska (1993), Comparison between Newtonian and non-Newtonian flow driven by internal loads, *Geophys. J. Int.*, *112*, 103–114, doi:10.1111/j.1365-246X.1993.tb01440.x.

Chase, C. G. (1972), The N plate problem of plate tectonics, *Geophys. J. R. Astron. Soc.*, *29*, 117–122.

Chase, C. G. (1978), Plate kinematics: The Americas, East Africa, and the rest of the world, *Earth Planet. Sci. Lett.*, *37*, 355–368, doi:10.1016/0012-821X(78)90051-1.

Christensen, U. R. (1984), Convection with pressure- and temperature-dependent non-Newtonian rheology, *Geophys. J. R. Astron. Soc.*, *77*, 343–384.

Conrad, C. P., and L. Husson (2009), Influence of dynamic topography on sea level and its rate of change, *Lithosphere*, *1*, 110–120, doi:10.1130/L32.1.

Conrad, C. P., and C. Lithgow-Bertelloni (2006), Influence of continental roots and asthenosphere on plate-mantle coupling, *Geophys. Res. Lett.*, *33*, L05312, doi:10.1029/2005GL025621.

Conrad, C. P., M. D. Behn, and P. G. Silver (2007), Global mantle flow and the development of seismic anisotropy: Differences between the oceanic and continental upper mantle, *J. Geophys. Res.*, *112*, B07317, doi:10.1029/2006JB004608.

Debayle, E., B. Kennett, and K. Priestley (2005), Global azimuthal seismic anisotropy and the unique plate-motion deformation of Australia, *Nature*, *433*, 509–512, doi:10.1038/nature03247.

DeMets, C., R. G. Gordon, D. F. Argus, and S. Stein (1994), Effects of recent revisions to the geomagnetic reversal time scale on estimates of current plate motions, *Geophys. Res. Lett.*, *21*, 2191–2194.

Di Giuseppe, E., C. Faccenna, F. Funiciello, J. van Hunen, and D. Giardini (2009), On the relations between trench migration, seafloor age, and the strength of the subducting lithosphere, *Lithosphere*, *1*, 121–128, doi:10.1130/L26.1.

DiVenere, V., and D. V. Kent (1999), Are the Pacific and Indo-Atlantic hotspots fixed? Testing the plate circuit through Antarctica, *Earth Planet. Sci. Lett.*, *170*, 105–117, doi:10.1016/S0012-821X(99)00096-5.

Doglioni, C., E. Carminati, M. Cuffaro, and D. Scrocca (2007), Subduction kinematics and dynamic constraints, *Earth Sci. Rev.*, *83*, 125–175, doi:10.1016/j.earscirev.2007.04.001.

Doubrovine, P., and J. A. Tarduno (2008), Linking the Late Cretaceous to Paleogene Pacific plate and Atlantic bordering continents using plate circuits and paleomagnetic data, *J. Geophys. Res.*, *113*, B07104, doi:10.1029/2008JB005584.

Ekström, G. (2001), Mappping azimuthal anisotropy of intermediate-period surface waves, *Eos Trans. AGU*, *82*(47), Fall Meet. Suppl., Abstract S51E-06.

Flesch, L. M., W. E. Holt, P. G. Silver, M. Stephenson, C.-Y. Wang, and W. W. Chan (2005), Constraining the extent of crust-mantle coupling in central Asia using GPS, geologic and shear wave splitting data, *Earth Planet. Sci. Lett.*, *238*, 248–268, doi:10.1016/j.epsl.2005.06.023.

Fontaine, F. R., E. E. E. Hooft, P. G. Burkett, D. R. Toomey, S. C. Solomon, and P. G. Silver (2005), Shear-wave splitting beneath the Galápagos archipelago, *Geophys. Res. Lett.*, *32*, L21308, doi:10.1029/2005GL024014.

Fouch, M. J., and S. Rondenay (2006), Seismic anisotropy beneath stable continental interiors, *Phys. Earth Planet. Inter.*, *158*, 292–320, doi:10.1016/j.pepi.2006.03.024.

Funiciello, F., C. Faccenna, A. Heuret, S. Lallemand, E. Di Giuseppe, and T. W. Becker (2008), Trench migration, slab migration, and slab-mantle coupling, *Earth Planet. Sci. Lett.*, *271*, 233–240, doi:10.1016/j.epsl.2008.04.006.

Gaboret, C., A. M. Forte, and J.-P. Montagner (2003), The unique dynamics of the Pacific Hemisphere mantle and its signature on seismic anisotropy, *Earth Planet. Sci. Lett.*, *208*, 219–233, doi:10.1016/S0012-821X(03)00037-2.

Gordon, R. G., and D. M. Jurdy (1986), Cenozoic global plate motions, *J. Geophys. Res.*, *91*, 12,389–12,406.

Gripp, A. E., and R. G. Gordon (1990), Current plate velocities relative to the hotspots incorporating the NUVEL-1 global plate motion model, *Geophys. Res. Lett.*, *17*, 1109–1112.

Gripp, A. E., and R. G. Gordon (2002), Young tracks of hotspots and current plate velocities, *Geophys. J. Int.*, *150*, 321–361, doi:10.1046/j.1365-246X.2002.01627.x.

Hamilton, W. B. (2003), An alternative Earth, *GSA Today*, *13*, 4–12, doi:10.1130/1052-5173(2003)013<0004:AAE>2.0.CO;2.

Hammond, J. O. S., J.-M. Kendall, G. Rumpker, J. Wookey, N. Teanby, P. Joseph, T. Ryberg, and G. Stuart (2005), Upper mantle anisotropy beneath the Seychelles microcontinent, *J. Geophys. Res.*, *110*, B11401, doi:10.1029/2005JB003757.

Hess, H. H. (1964), Seismic anisotropy of the uppermost mantle under oceans, *Nature*, *203*, 629–631, doi:10.1038/203629a0.

Heuret, A., and S. Lallemand (2005), Plate motions, slab dynamics and back-arc deformation, *Phys. Earth Planet. Inter.*, *149*, 31–51, doi:10.1016/j.pepi.2004.08.022.

Husson, L., C. P. Conrad, and C. Faccenna (2008), Tethyan closure, Andean orogeny, and westward drift of the Pacific basin, *Earth Planet. Sci. Lett.*, *271*, 303–310, doi:10.1016/j.epsl.2008.04.022.

Jordan, T. H. (1975), The continental tectosphere, *Rev. Geophys.*, *13*, 1–12, doi:10.1029/RG013i003p00001.

Kaminski, E., and N. M. Ribe (2002), Timescales for the evolution of seismic anisotropy in mantle flow, *Geochem. Geophys. Geosyst.*, *3*(8), 1051, doi:10.1029/2001GC000222.

Karato, S., and B. B. Karki (2001), Origin of lateral variation of seismic wave velocities and density in the deep mantle, *J. Geophys. Res.*, *106*, 21771–21783.

Karato, S., and P. Wu (1993), Rheology of the upper mantle: A synthesis, *Science*, *260*, 771–778, doi:10.1126/science.260.5109.771.

Klosko, E. R., R. M. Russo, E. A. Okal, and W. P. Richardson (2001), Evidence for a rheologically strong chemical mantle root beneath the Ontong-Java Plateau, *Earth Planet. Sci. Lett.*, *186*, 347–361, doi:10.1016/S0012-821X(01)00235-7.

Kreemer, C. (2009), Absolute plate motions constrained by shear wave splitting orientations with implications for hot spot motions and mantle flow, *J. Geophys. Res.*, *114*, B10405, doi:10.1029/2009JB006416.

Kreemer, C., W. E. Holt, and A. J. Haines (2003), An integrated global model of present-day plate motions and plate boundary deformation, *Geophys. J. Int.*, *154*, 8–34, doi:10.1046/j.1365-246X.2003.01917.x.

Kreemer, C., D. A. Lavallée, G. Blewitt, and W. E. Holt (2006), On the stability of a geodetic no-net-rotation frame and its implications for the International Terrestrial Reference Frame, *Geophys. Res. Lett.*, *33*, L17306, doi:10.1029/2006GL027058.

Lallemand, S., A. Heuret, and D. Boutelier (2005), On the relationships between slab dip, back-arc stress, upper plate absolute motion, and crustal nature in subduction zones, *Geochem. Geophys. Geosyst.*, *6*, Q09006, doi:10.1029/2005GC000917.

Lallemand, S., A. Heuret, C. Faccenna, and F. Funiciello (2008), Subduction dynamics as revealed by trench migration, *Tectonics*, *27*, TC3014, doi:10.1029/2007TC002212.

Lithgow-Bertelloni, C., and P. G. Silver (1998), Dynamic topography, plate driving forces and the Africa superswell, *Nature*, *395*, 269–272, doi:10.1038/26212.

Long, M. D., and P. G. Silver (2009), Mantle flow in subduction systems: The subslab flow field and implications for mantle dynamics, *J. Geophys. Res.*, *114*, B10312, doi:10.1029/2008JB006200.

McKenzie, D. (1979), Finite deformation during fluid flow, *Geophys. J. R. Astron. Soc.*, *58*, 689–715.

Minster, J. B., and T. H. Jordan (1978), Present-day plate motions, *J. Geophys. Res.*, *83*, 5331–5354, doi:10.1029/JB083iB11p05331.

Mitrovica, J. X. (1996), Haskell [1935] revisited, *J. Geophys. Res.*, *101*, 555–569, doi:10.1029/95JB03208.

Molnar, P., and J. Stock (1987), Relative motions of hotspots in the Pacific, Atlantic, and Indian oceans since Late Cretaceous time, *Nature*, *327*, 587–591, doi:10.1038/327587a0.

Montagner, J.-P. (1994), Can seismology tell us anything about convection in the mantle?, *Rev. Geophys.*, *32*, 115–137, doi:10.1029/94RG00099.

Morgan, W. J. (1968), Rises, trenches, great faults, and crustal blocks, *J. Geophys. Res.*, *73*, 1959–1982, doi:10.1029/JB073i006p01959.

Morgan, W. J. (1972), Deep mantle convection plumes and plate motions, *Am. Assoc. Pet. Geol. Bull.*, *56*, 203–213.

Müller, R. D., J.-Y. Royer, and L. A. Lawver (1993), Revised plate mot ions relative to the hotspots from combined Atlantic and Indian Ocean hotspot tracks, *Geology*, *16*, 275–278.

Nagel, T. J., W. B. F. Ryan, A. Malinverno, and W. R. Buck (2008), Pacific trench motions controlled by the asymmetric plate configuration, *Tectonics*, *27*, TC3005, doi:10.1029/2007TC002183.

O'Neill, C., D. Müller, and B. Steinberger (2005), On the uncertainties in hot spot reconstructions and the significance of moving hot spot reference frames, *Geochem. Geophys. Geosyst.*, *6*, Q04003, doi:10.1029/2004GC000784.

Paulson, A., S. Zhong, and J. Wahr (2007), Inference of mantle viscosity from GRACE and relative sea level data, *Geophys. J. Int.*, *171*, 497–508, doi:10.1111/j.1365-246X.2007.03556.x.

Ribe, N. M. (1989), Seismic anisotropy and mantle flow, *J. Geophys. Res.*, *94*, 4213–4223, doi:10.1029/JB094iB04p04213.

Ricard, Y., C. Doglioni, and R. Sabadini (1991), Differential rotation between lithosphere and mantle: A consequence of lateral mantle viscosity variations, *J. Geophys. Res.*, *96*, 8407–8415, doi:10.1029/91JB00204.

Ritsema, J., H. J. van Heijst, and J. H. Woodhouse (2004), Global transition zone tomography, *J. Geophys. Res.*, *109*, B02302, doi:10.1029/2003JB002610.

Savage, M. K. (1999), Seismic anisotropy and mantle deformation: What have we learned from shear wave splitting?, *Rev. Geophys.*, *37*, 65–106, doi:10.1029/98RG02075.

Schellart, W. P., D. R. Stegman, and J. Freeman (2008), Global trench migration velocities and slab migration induced upper mantle volume fluxes: Constraints to find an Earth reference frame based on minimizing viscous dissipation, *Earth Sci. Rev.*, *88*, 118–144, doi:10.1016/j.earscirev.2008.01.005.

Sella, G. F., T. H. Dixon, and A. Mao (2002), REVEL: A model for Recent plate velocities from space geodesy, *J. Geophys. Res.*, *107*(B4), 2081, doi:10.1029/2000JB000033.

Silver, P. G. (1996), Seismic anisotropy beneath the continents: Probing the depths of geology, *Annu. Rev. Earth Planet. Sci.*, *24*, 385–432, doi:10.1146/annurev.earth.24.1.385.

Silver, P. G., and W. W. Chan (1988), Implications for continental structure and evolution from seismic anisotropy, *Nature*, *335*, 34–39, doi:10.1038/335034a0.

Silver, P. G., and W. E. Holt (2002), The mantle flow field beneath western North America, *Science*, *295*, 1054–1057, doi:10.1126/science.1066878.

Silver, P. G., M. J. Fouch, S. S. Gao, and M. Schmitz (2004), Seismic anisotropy, mantle fabric, and the magmatic evolution of Precambrian southern Africa, *S. Afr. J. Geol.*, *107*, 45–58, doi:10.2113/107.1-2.45.

Smith, G. P., D. A. Wiens, K. M. Fischer, L. M. Dorman, S. C. Webb, and J. A. Hildebrand (2001), A complex pattern of mantle flow in the Lau backarc, *Science*, *292*, 713–716, doi:10.1126/science.1058763.

Solomon, S. C., and N. H. Sleep (1974), Some simple physical models for absolute plate motions, *J. Geophys. Res.*, *79*, 2557–2567, doi:10.1029/JB079i017p02557.

Spasojevic, S., L. Liu, and M. Gurnis (2009), Adjoint models of mantle convection with seismic, plate motion, and stratigraphic constraints: North America since the Late Cretaceous, *Geochem. Geophys. Geosyst.*, *10*, Q05W02, doi:10.1029/2008GC002345.

Steinberger, B. (2000), Plumes in a convecting mantle: Models and observations for individual hotspots, *J. Geophys. Res.*, *105*, 11,127–11,152, doi:10.1029/1999JB900398.

Steinberger, B. (2002), Motion of the Easter hot spot relative to Hawaii and Louisville hot spots, *Geochem. Geophys. Geosyst.*, *3*(11), 8503, doi:10.1029/2002GC000334.

Steinberger, B., R. Sutherland, and R. J. O'Connell (2004), Prediction of Emperor-Hawaii seamount locations from a revised model of global plate motion and mantle flow, *Nature*, *430*, 167–173, doi:10.1038/nature02660.

Tan, E., E. Choi, P. Thoutireddy, M. Gurnis, and M. Aivazis (2006), GeoFramework: Coupling multiple models of mantle convection within a computational framework, *Geochem. Geophys. Geosyst.*, *7*, Q06001, doi:10.1029/2005GC001155.

Tarduno, J. A., and R. D. Cottrell (1997), Paleomagnetic evidence for motion of the Hawaiian hotspot during formation of the Emperor seamounts, *Earth Planet. Sci. Lett.*, *153*, 171–180, doi:10.1016/S0012-821X(97)00169-6.

Tarduno, J. A., and J. Gee (1995), Large-scale motion between Pacific and Atlantic hotspots, *Nature*, *378*, 477–480, doi:10.1038/378477a0.

Tarduno, J. A., et al. (2003), The Emperor Seamounts: Southward motion of the Hawaiian hotspot plume in Earth's mantle, *Science*, *301*, 1064–1069, doi:10.1126/science.1086442.

Tarduno, J., H.-P. Bunge, N. Sleep, and U. Hansen (2009), The bent Hawaiian-Emperor hotspot track: Inheriting the mantle wind, *Science*, *324*, 50–53, doi:10.1126/science.1161256.

Torsvik, T. H., R. D. Muller, R. Van der Voo, B. Steinberger, and C. Gaina (2008), Global plate motion frames: Toward a unified model, *Rev. Geophys.*, *46*, RG3004, doi:10.1029/2007RG000227.

Torsvik, T. H., B. Steinberger, M. Gurnis, and C. Gaina (2010), Plate tectonics and net lithosphere rotation over the past 150 My, *Earth Planet. Sci. Lett.*, *291*, 106–112, doi:10.1016/j.epsl.2009.12.055.

Trampert, J., and J. H. Woodhouse (2003), Global anisotropic phase velocity maps for the fundamental mode surface waves between 40 and 150 s, *Geophys. J. Int.*, *154*, 154–165, doi:10.1046/j.1365-246X.2003.01952.x.

van der Meer, D. G., W. Spakman, D. J. J. van Hinsbergen, M. L. Amaru, and T. H. Torsvik (2010), Towards absolute plate motions constrained by lower-mantle slab remnants, *Nat. Geosci.*, *3*, 36–40, doi:10.1038/ngeo708.

van Hunen, J., and O. Cadek (2009), Reduced oceanic seismic anisotropy by small-scale convection, *Earth Planet. Sci. Lett.*, *284*, 622–629, doi:10.1016/j.epsl.2009.05.034.

Vine, F. J., and D. H. Matthews (1963), Magnetic anomalies over oceanic ridges, *Nature*, *199*, 947–949, doi:10.1038/199947a0.

Wang, S., and R. Wang (2001), Current plate velocities relative to hotspots: Implications for hotspot motion, mantle viscosity and global reference frame, *Earth Planet. Sci. Lett.*, *189*, 133–140, doi:10.1016/S0012-821X(01)00351-X.

Wessel, P., Y. Harada, and L. W. Kroenke (2006), Toward a self-consistent, high-resolution absolute plate motion model for the Pacific, *Geochem. Geophys. Geosyst.*, *7*, Q03L12, doi:10.1029/2005GC001000.

Wilson, J. T. (1965), Evidence from ocean islands suggesting movement in the Earth, in *Symposium on Continental Drift*, *Philos. Trans. R. Soc. London, Ser. A*, *258*, 145–167.

Wolfe, C. J., and P. G. Silver (1998), Seismic anisotropy of oceanic upper mantle: Shear wave splitting methodologies and observations, *J. Geophys. Res.*, *103*, 749–771, doi:10.1029/97JB02023.

Zhong, S. (2001), Role of ocean-continent contrast and continental keels on plate motion, net rotation of lithosphere, and the geoid, *J. Geophys. Res.*, *106*, 703–712, doi:10.1029/2000JB900364.

Zhong, S., M. T. Zuber, L. N. Moresi, and M. Gurnis (2000), The role of temperature-dependent viscosity and surface plates in spherical shell models of mantle convection, *J. Geophys. Res.*, *105*, 11,063–11,082.